Society For Biomaterials

A simplified *in vivo* approach for evaluating the bioabsorbable behavior of candidate stent materials

Daniel Pierson,[1] Jacob Edick,[2] Aaron Tauscher,[1] Ellen Pokorney,[1] Patrick Bowen,[2] Jesse Gelbaugh,[2] Jon Stinson,[3] Heather Getty,[3] Chee Huei Lee,[4] Jaroslaw Drelich,[2] Jeremy Goldman[1]

[1]Department of Biomedical Engineering, Michigan Technological University, Houghton, Michigan 49931-1295
[2]Department of Materials Science and Engineering, Michigan Technological University, Houghton, Michigan 49931-1295
[3]Boston Scientific Corporation, Maple Grove, Minnesota 55311-1566
[4]Department of Physics, Michigan Technological University, Houghton, Michigan 49931-1295

Received 10 January 2011; revised 3 May 2011; accepted 21 June 2011
Published online 8 September 2011 in Wiley Online Library (wileyonlinelibrary.com). DOI: 10.1002/jbm.b.31922

Abstract: Metal stents are commonly used to revascularize occluded arteries. A bioabsorbable metal stent that harmlessly erodes away over time may minimize the normal chronic risks associated with permanent implants. However, there is no simple, low-cost method of introducing candidate materials into the arterial environment. Here, we developed a novel experimental model where a biomaterial wire is implanted into a rat artery lumen (simulating bioabsorbable stent blood contact) or artery wall (simulating bioabsorbable stent matrix contact). We use this model to clarify the corrosion mechanism of iron ($\geq$99.5 wt %), which is a candidate bioabsorbable stent material due to its biocompatibility and mechanical strength. We found that iron wire encapsulation within the arterial wall extracellular matrix resulted in substantial biocorrosion by 22 days, with a voluminous corrosion product retained within the vessel wall at 9 months. In contrast, the blood-contacting luminal implant experienced minimal biocorrosion at 9 months. The importance of arterial blood versus arterial wall contact for regulating biocorrosion was confirmed with magnesium wires. We found that magnesium was highly corroded when placed in the arterial wall but was not corroded when exposed to blood in the arterial lumen for 3 weeks. The results demonstrate the capability of the vascular implantation model to conduct rapid *in vivo* assessments of vascular biomaterial corrosion behavior and to predict long-term biocorrosion behavior from material analyses. The results also highlight the critical role of the arterial environment (blood vs. matrix contact) in directing the corrosion behavior of biodegradable metals. J Biomed Mater Res Part B: Appl Biomater 100B: 58–67, 2012.

Key Words: vascular stents, blood–material interaction, biodegradation, biocompatibility/soft tissue

How to cite this article: Pierson D, Edick J, Tauscher A, Pokorney E, Bowen P, Gelbaugh J, Stinson J, Getty H, Lee CH, Drelich J, Goldman J. 2012. A simplified in vivo approach for evaluating the bioabsorbable behavior of candidate stent materials. J Biomed Mater Res Part B 2012:100B:58–67.

INTRODUCTION

Vascular stents are metal scaffolds used to prop open atherosclerotic blood vessels and improve blood flow. Nonabsorbable stents are permanent implants.[1–3] Unfortunately, the biological and mechanical environment of the vessel may challenge the long-term integrity of permanent stents. However, it has been hypothesized that stents placed in many atherosclerotic arteries may require only about 3–6 months of mechanical integrity for scaffolding. Bioabsorbable or biodegradable stents that provide mechanical support during vascular wall repair and then harmlessly erode after the vascular wall has stabilized may eliminate some of the potential chronic risks of permanent stents and may mitigate the complexity of repeat stenting at the same site in the event of restenosis.[4–8]

Current efforts to develop a bioabsorbable or biodegradable stent have focused on magnesium based alloys,[9–12] poly-L-lactic acid (PLLA) polymers,[13–15] and high-weight percent iron.[16–19] Magnesium and iron stents degrade into physiological products, are immunologically inert, and possess physical properties that are more similar to commercial stainless steel stents and cobalt chromium alloys than polymer bioabsorbable stent candidate materials.[7,20,21] In contrast to iron, which experiences a relatively slow rate of

Additional Supporting Information may be found in the online version of this article.
Conflict of interest: No benefit of any kind will be received either directly or indirectly by the authors.
Correspondence to: J. Goldman; e-mail: jgoldman@mtu.edu
Contract grant sponsor: Boston Scientific Corporation and National Institutes of Health; contract grant number: R21-HL-093568 and R15-HL-093705

degradation, magnesium and PLLA stents experience a higher rate of degradation following deployment that can result in premature loss of mechanical integrity and early-vascular recoil.[21] Furthermore, whereas iron stents are radio-opaque, magnesium and polymer stents are not visible on an angiogram, which may hinder stent implantation.[7,21] Polymer stents have further limitations including a greater potential for tissue incompatibility[14] and the inability to fully expand with the use of balloon dilatation. Due to their lower radial force compared with their stainless steel counterparts, a greater thickness is required for polymer stents.[10] Although iron possesses more ideal properties compared with magnesium and polymer materials, the slow degradation rate of iron may result in an extended presence of iron stents in the artery.[22] Thus, iron materials may need to be modified to produce a more suitable degradation rate.

Presently, there is no simple, low-cost method of introducing candidate stent materials into the arterial environment, necessitating reliance on unrealistic *in vitro* models or costly and time-consuming large animal stent implantation studies. Here, we have developed a novel *in vivo* model for the early-*in vivo* evaluation of candidate stent materials. In this model, candidate stent materials are drawn into a wire and implanted into the rat abdominal aorta wall or lumen to simulate a stent implantation. We demonstrate the capability of this model by providing insight into the mechanism of iron degradation *in vivo*.

MATERIALS AND METHODS

Male Sprague Dawley rats from Harlan Labs were used in the animal experiments. All animal experiments were approved by the animal care and use committee of Michigan Technological University. NIH guidelines for the care and use of laboratory animals (NIH Publication #85-23 Rev. 1985) have been observed.

Wire sterilization

Before implantation, iron wires were cleaned in a ProCleaner™ cleaning device (BioForce Nanosciences; Ames, IA) for 30 min. ProCleaner™ device is equipped with a high-intensity mercury vapor lamp generating UV illumination that converts oxygen into ozone, which attacks and removes molecular levels of organic contamination from small samples.

Aortic implantation

Sprague Dawley rats (Harlan Labs) anesthetized with isoflurane in oxygen gas were surgically implanted with annealed iron wire of 99.99+ wt % and 0.25 mm diameter or magnesium wire of 99.9+ wt % and 0.25 mm diameter (Goodfellow Corporation). Two different wire implantation models were used, a wall implant and a luminal implant. In both models, a 2-cm long sterilized metal wire was punctured into the abdominal aorta. For the aortic wall implants, the arterial adventitia was punctured with the metal wire, which was then led a distance of 15 mm within the adventitia. This wire was firmly embedded in the extracellular matrix of the adventitia and did not become dislocated. For the luminal implants, the artery was punctured with the wire, which was then led into the lumen for a distance of approximately 15 mm before puncturing the wall a second time to exteriorize the wire from the artery. Because the luminal wire implant became encapsulated in neointimal-like tissue at late time points, we also implanted wires into the lumen with the wire bowed away from the endothelium. Thus, when luminally implanted, the wire was placed in gentle contact with the vessel wall, and in some cases, it was bowed away from the vessel wall. The wires that were bowed away from the vessel wall remained free from encapsulation in neointimal-like tissue. This approach allowed us to inspect luminal wires in the presence and absence of neointimal-like tissue encapsulation. Following implantation, the portion of the wire remaining outside the artery at both ends was slightly bent to prevent dislocation. After 22 days, 1.5, 3, 4.5, or 9 months, the rats were euthanized using carbon dioxide asphyxiation, and the wires or aortas containing the implanted wires were harvested for analysis.

Histology

Rat aortas containing the iron wire implants were snap-frozen in liquid nitrogen and cryo-sectioned for histological analysis. Samples were preserved in a -80°C freezer before staining. The samples were stained with hematoxylin and eosin, mounted in Permount solution, and imaged using an Olympus BX51, DP70 brightfield microscope.

Raman spectroscopy

A Jobin-Yvon Lab RAM HR800 Raman Spectrometer was used to analyze the corrosion products. The laser beam (wavelength 632 nm) was focused onto the sample to analyze the resulting energy level of light reflected back to the detector. The amount of energy absorption by the bonds present within the sample creates the position and intensity of the characteristic peaks from the sample. Scans were performed from a minimum value of 100 cm^{-1} to a maximum value that varied between 1000 and 1500 cm^{-1}. The resulting peaks were compared with standard peaks of known minerals for identification.

Scanning electron microscopy/energy dispersive X-ray spectroscopy

The surface morphology and elemental analysis of iron samples were carried out using the JEOL JSM 6400 Scanning electron microscopy (SEM) equipped with energy dispersive spectrometer (EDS). The accelerating voltage used for all samples was 20 kV and 39 mm working distance. Samples requiring images of the wires in cross section were mounted in epoxy [AeroMarine Epoxy Resin #300 and AeroMarine 'Non-Blushing' Cycloaliphatic Epoxy Hardener #21 at a 2:1 weight ratio (AeroMarine Products; San Diego, CA)]. Wires with corrosion product on the surface were held vertically using super glue to prevent damage to the corrosion product. The wires were glued to a small piece of heavy paper using Loctite superglue. Fine tip tweezers were used to hold the wires in place until the superglue cured. Once cured the small piece of paper was then placed in a

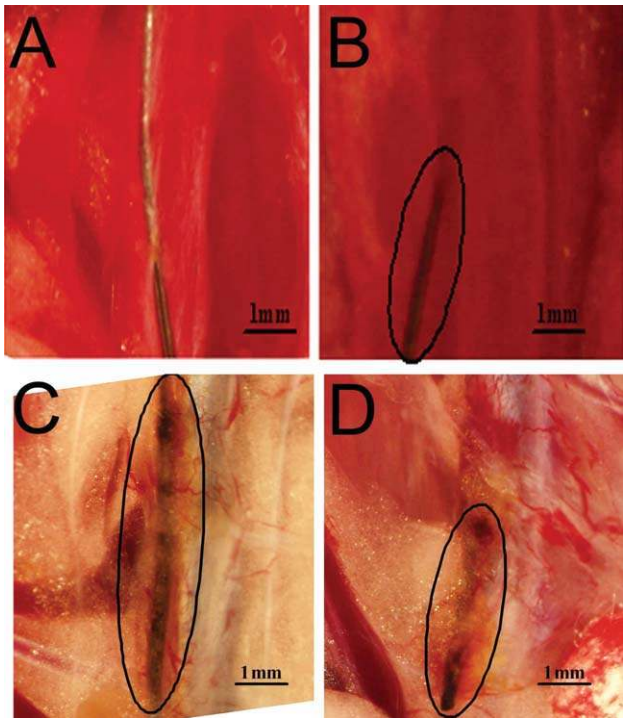

FIGURE 1. Implantation of iron wire into rat aortic wall (A) and lumen (B—visible exterior wire is circled). Explanation of the iron wire after 22 days demonstrates a prominent rust cloud surrounding the artery wall wire implant (C) and around the visible portion of the luminally implanted wire (D). The majority of the luminally implanted wire was present within the arterial lumen. $n = 2$ per condition. Scale bar in each image = 1 mm. [Color figure can be viewed in the online issue, which is available at wileyonlinelibrary.com.]

mounting cup, and the AeroMarine epoxy and hardener were then added and allowed to cure overnight. The samples were then cross sectioned and polished using 60, 120, 240, 400, and 600 grit sandpapers in series. The fine polishing was carried out using a 6 μm diamond cloth and 0.5 μm alumina particles, in sequence.

RESULTS

Tissue discoloration from the iron wire implanted within the arterial wall

Brightfield images of the implanted iron wires were collected immediately following implantation [Figure 1(A,B)] and before explanation at 22 days [Figure 1(C,D)]. The artery wall wire implant produced a brown-colored product in the tissue surrounding the wire [Figure 1(C)]. The luminal wire did not produce visible corrosion product, although the same brown corrosion product was present around the exteriorized portion of the wire [Figure 1(D)]. Thus, in both models, corrosion product was observed on iron wire surrounded by biological tissue, but not on wire surrounded by flowing arterial blood.

Pitting and corrosion product dispersion on the iron wire implanted into the arterial wall

Surface morphology of the 22-day explanted iron was investigated using SEM. The extracted samples were placed in a sonicator to remove attached biological tissue to produce an accurate projection of the material surface. SEM images of the clean wire before implantation and of wires obtained following explanation from the two *in vivo* models were collected. These images showed a similar surface appearance between the clean wire and the wire harvested from the arterial lumen [Figure 2(A,B)].

A comparison of the clean wire [Figure 2(A)] with the artery wall wire implant [Figure 2(C)] demonstrated a marked difference in the surface topography. Portions of the wire in Figure 2(C) covered in tissue appear darker. The lighter areas of the image are portions of the wire where the tissue was removed as a result of sonification. These areas show a heavy amount of pitting on the surface of the sample. The SEM image at 10,000× [Figure 2(D)] shows a nonuniform attack producing a maximum pit depth of 1–2 μm. Thus, the luminal wire resisted corrosion, whereas the wall wire experienced substantial corrosion.

Cross sections of the implanted wires along with host artery were hemotoxylin and eosin stained and inspected to compare degradation product distribution throughout the tissue that surrounded the wire implants. Figure 3(A,B) depicts an iron wire implanted into the arterial wall for 22 days. The corrosion product was present in clusters that dispersed a maximum distance of 450 μm away from the original wire location [as indicated by the red circles in Figure 3(B)]. In contrast, the corrosion product produced from the 22-day luminal wire implants traveled much shorter distances [Figure 3(C)] and were observed to disperse a maximum of 75 μm away from the wire. A thin film visible around the luminal wire implants had a highly concentrated rust discoloration [Figure 3(C)—green arrows], suggesting that a passive layer may have formed around the wires placed in contact with flowing blood.

Increased corrosion from the iron wires placed in long-term contact with the arterial wall matrix. Wires were also implanted into the artery for 9 months to evaluate long-term iron biodegradation. Explanted wires and artery were cross sectioned for histological analysis. It was found that iron wires implanted into the arterial lumen against the endothelium experienced minimal biocorrosion despite substantial encapsulation in neointimal-like tissue [Figure 4(A)]. In contrast, iron wires implanted into the arterial wall for 9 months experienced extensive biodegradation [Figure 4(B)], with the original wire structure substantially disintegrated into voluminous flakes that appeared to have compromised the integrity of the arterial wall. Although cross sections of iron wires implanted into the arterial lumen against the endothelium revealed a well preserved iron wire [Figure 4(A)], cross sections of the same wires at the artery wall puncture sites contained similar voluminous degradation product as was seen on wires implanted for the same amount of time in the arterial wall (data not shown). Wires that were bowed out away from the endothelium in the arterial lumen for 9 months were intact on opening the artery and exposing the interior contents. Yellow arrow in Figure 4(C) identifies tissue encapsulation-free wire region

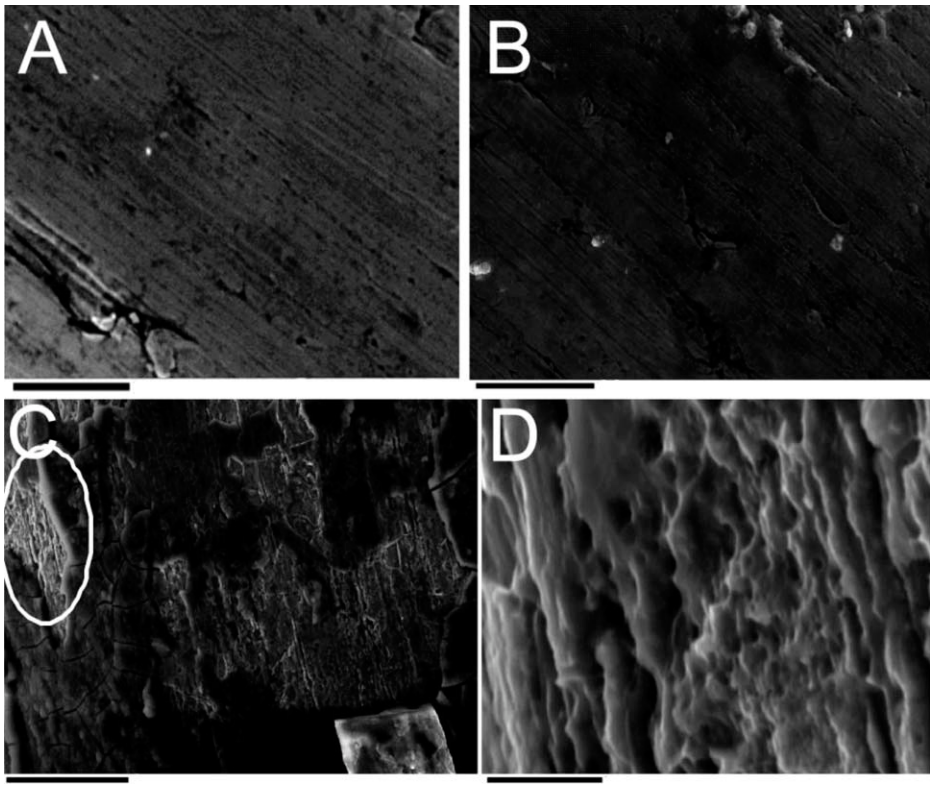

FIGURE 2. SEM images of clean iron wire (A) and implanted wire after 22 days within the arterial lumen (B) and wall (C). The clean wire before implantation (A) is visibly indistinguishable from the arterial lumen wire implant (B). In contrast, moderate pitting is evident on the arterial wall wire implant (C—circled region). High magnification of the circled region from image C is shown (D). Scale bar in images (A)–(C) = 30 μm and in image (D) = 3 μm.

that was bowed out into the lumen, away from the arterial wall. In contrast, the arterial wall penetration sites had substantially degraded. Green arrows in Figure 4(C) identify tapered corrosion product near sites where the wire was punctured through the arterial wall. Wires implanted for 9 months into the arterial wall or in the lumen against the endothelium could not be withdrawn undamaged from the artery, due to the extensive disintegration of the wire that had occurred at the matrix-contacting surfaces. In summary, wire surfaces placed in initial contact with arterial blood flow were well preserved over 9 months irrespective of whether the wire became encapsulated in neointimal-like tissue or remained free of neointimal growth, whereas wire surfaces placed in contact with the arterial wall matrix were substantially degraded.

Progressive biocorrosion by arterial wall matrix contact. Iron wires placed in the arterial wall were explanted at 1.5 and 3 months and inspected with a high-magnification stereomicroscope to compare the degree of discoloration and biocorrosion with wires placed in the arterial lumen and bowed away from the wall to prevent neointimal-like tissue encapsulation for 9 months. Discoloration was evident on the wall wire implant as early as 1.5 months [Figure 5(B)] relative to a nonimplanted iron wire [Figure 5(A)]. Diameter expansion and irregular surface contours on the wire were visible on 3-month wall wire explants [Figure 5(C)]. In contrast to the corrosion behavior of the wall wire implants, blood-contacting surfaces of the luminal wire implants were resistant to corrosion, whereas matrix-contacting surfaces of the luminal wires (i.e., surfaces present at the artery wall puncture sites) were highly corroded [Figure 5(D,E), respectively]. Wires implanted for 4.5 or 9 months into the artery wall or for 9 months against the endothelium of the lumen could not be withdrawn from the artery without damaging the wire (due to matrix encapsulation and extensive iron degradation) and were not suitable for comparison with the wires shown in Figure 5. The results from inspecting the intact wires are consistent with the histological data.

Confirmation of divergent corrosion behavior of biodegradable metals placed in the lumen and arterial wall. To determine whether the distinct corrosion processes we observed in the arterial lumen and wall were specific to iron or were specific to the arterial environments, we implanted magnesium wires into the same arterial environments as was done for the iron wires. We found that arterial wall contact caused extensive biocorrosion of the magnesium wire, with extensive and nonuniform local reactions occurring on the wire surface as early as 3 weeks [Figure 5(G,H)] relative to clean magnesium wires [Figure 5(F)].

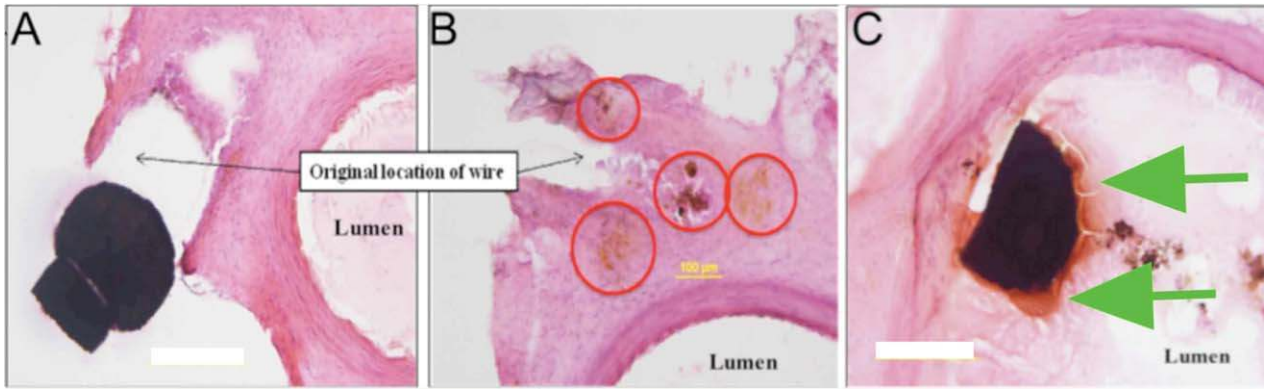

FIGURE 3. Histological analysis of the 22-day wire implants. Hematoxylin/eosin stained tissue sections depict the location of the iron wire and corrosion product within the arterial wall (A and B) and lumen (C). The black circular structure is the iron wire cross section. Note that the iron wire became dislocated during sectioning and the black arrow in (A) and (B) identifies the original wire location. The circled areas in image (B) identify corrosion product clusters. A thin rust-colored film surrounds the luminal wire cross section (C—green arrows). $n = 2$ per condition. Scale bar in (A) and (C) = 200 μm. [Color figure can be viewed in the online issue, which is available at wileyonlinelibrary.com.]

The *in situ* image of the magnesium wire [Figure 5(G)] depicts a lack of visible corrosion product within the arterial matrix. There is evidence of nonuniform erosion [pits on the wire surface are identified by green arrows in Figure 5(H)], with at least one fragmentation point present in 2 out of 3 wires evaluated at 3 weeks [typical fragmentation shown by the yellow arrow in Figure 5(G)]. The fragmentation of the magnesium wires may have been a consequence of extensive pitting corrosion. In contrast to magnesium wires, none of the iron wires had experienced a fragmentation event, even at 9 months. In contrast to iron, there was no retention of corrosion product in the biological tissue surrounding the magnesium wires. Similar to what was found with luminal iron wires, luminal magnesium wires

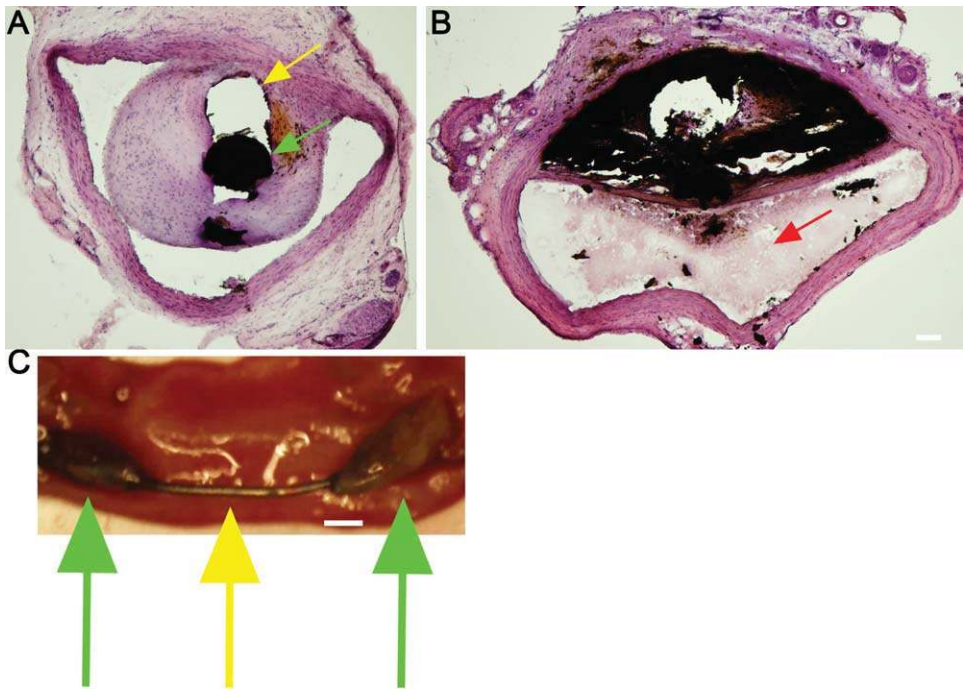

FIGURE 4. Histological analysis of the 9-month wire implants. Hematoxylin/eosin stained tissue sections depict the location of the iron wire and corrosion product within the arterial lumen (A) and wall (B). The black circular structure in (A) is the iron wire cross section (identified by the green arrow). Note that the iron wire became dislocated during sectioning and the yellow arrow in (A) identifies the original wire location, which was placed gently against the vessel wall. The 9-month luminal wire is well preserved from biodegradation (A). In contrast, the 9-month wall wire implant is substantially biodegraded (B). When the luminal wire was bowed out away from the vessel wall, the central portion of the wire (yellow arrow in C) remained free of encapsulating tissue and experienced minimal biodegradation. In contrast, the wall puncture sites (green arrows in C) experienced substantial degradation. Red layer in (C) background is the luminal surface of the exposed artery. Scale bar in (B) is 100 μm and (C) is 1 mm. $n = 2$ per condition. [Color figure can be viewed in the online issue, which is available at wileyonlinelibrary.com.]

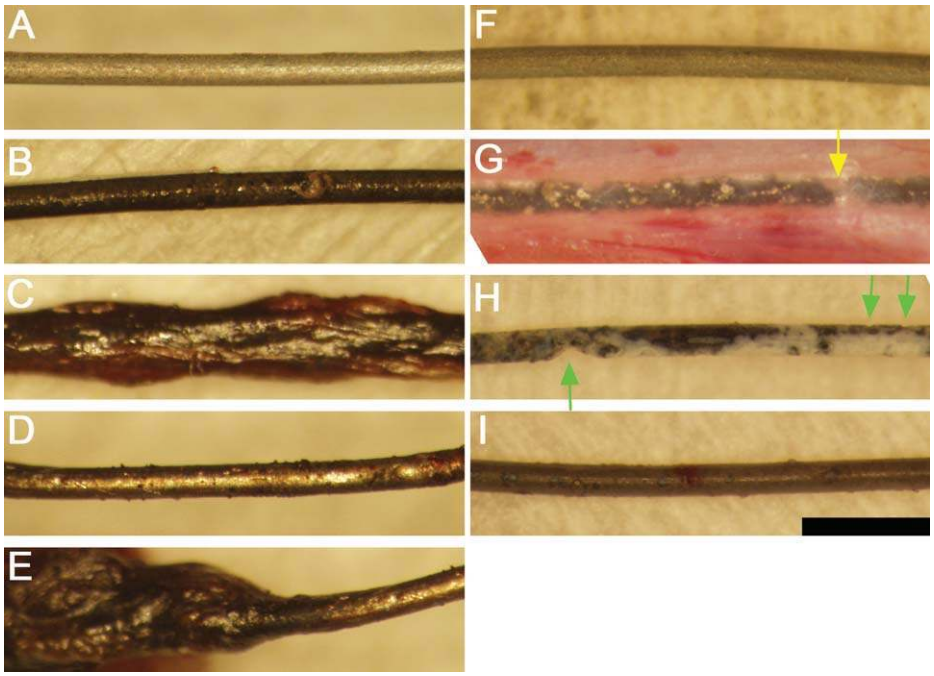

FIGURE 5. Extent of corrosion compared between intact wires. Clean iron wire (A) and wires explanted from the arterial wall at 1.5 (B) and 3 (C) months were compared with wires explanted from the lumen at 9 months, at central (D) or wall locations (E), to assess differences in the degree of biocorrosion. Clean magnesium wire (F), magnesium wires placed in the arterial wall for 3 weeks before and subsequent to explanation (G and H, respectively), and magnesium wires placed in blood contact for 3 weeks (I). Scale bar in (I) is 1 mm. For the iron, $n = 4$ for 1.5 and 3-month wall specimens and $n = 2$ for 9-month specimens. For the magnesium, $n = 3$ for both 3-week wall and lumen specimens. [Color figure can be viewed in the online issue, which is available at wileyonlinelibrary.com.]

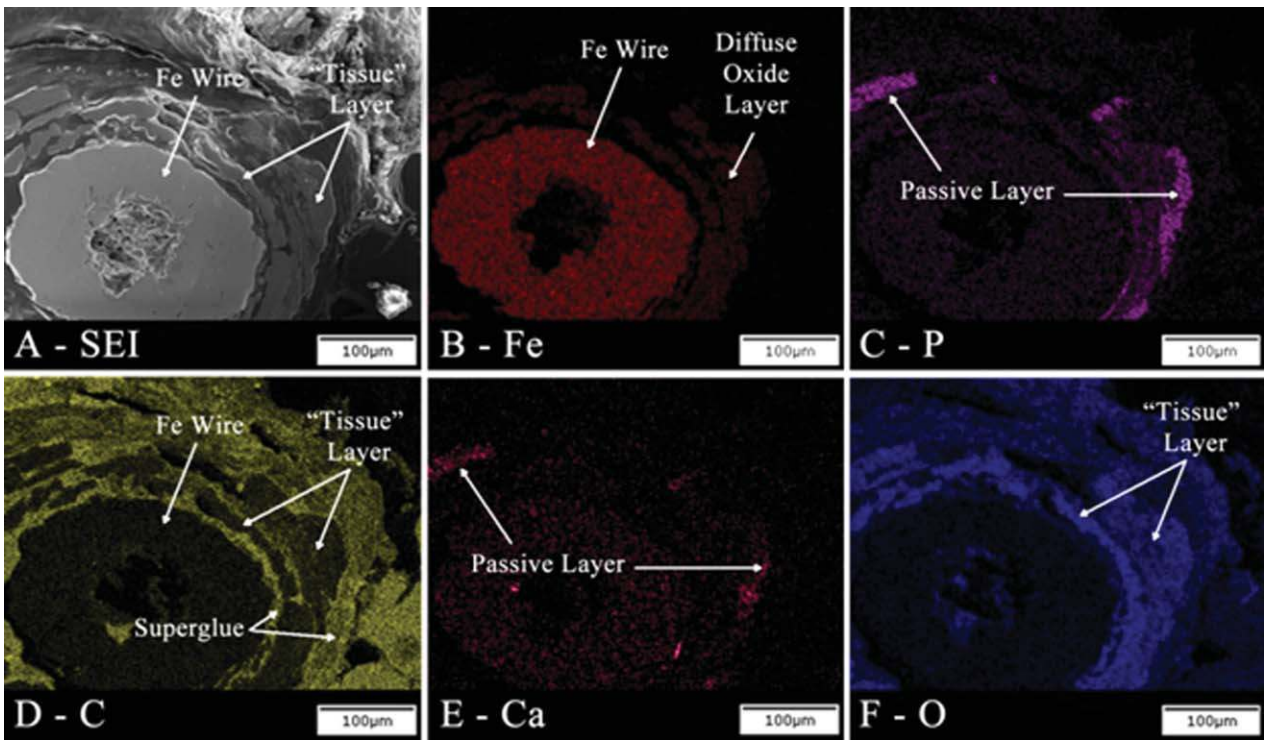

FIGURE 6. X-ray maps of a cross-sectioned 9-month iron wire explanted from the arterial wall. A secondary electron image of the area examined is shown (A) as well as X-ray maps of iron (B), phosphorus (C), carbon (D), calcium (E), and oxygen (F). Scale bar shown in each image is 100 μm. [Color figure can be viewed in the online issue, which is available at wileyonlinelibrary.com.]

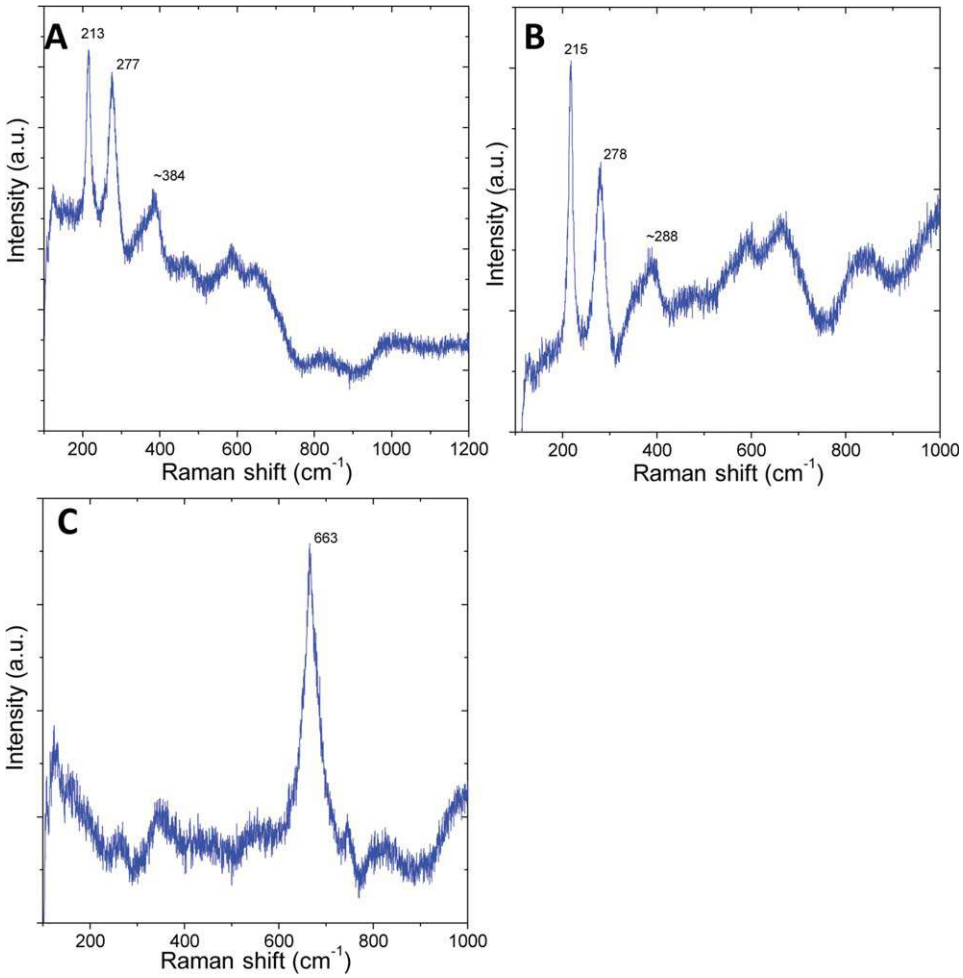

FIGURE 7. Raman spectrum for aortic rat model wire explants. The spectrum from all wire implants, within the artery wall (A) and inside the lumen (B and C—same specimen), identified hematite as the corrosion product. [Color figure can be viewed in the online issue, which is available at wileyonlinelibrary.com.]

appeared to have resisted corrosion [Figure 5(I)]. This appeared to be the case because no pits and a relatively uniform surface coloration were evident on the magnesium wire surface placed in contact with blood.

Elemental analysis of the 9-month iron wire at the arterial wall. Corroded iron wires were characterized using EDS with the goal of identifying the elemental constituents of the corrosion products. After being cross sectioned and polished, elemental mapping was performed on the 9-month iron sample from the arterial wall location (Figure 6). The layer surrounding the metallic surface apparent as a light gray band on the secondary electron image (SEI) in [Figure 6(A)]—is composed of an unknown matrix component, an iron oxide component, and a calcium- and phosphorus-bearing phase. Evidence for the matrix component comes from the carbon and oxygen compositional maps. The above-background amount of carbon and oxygen shown in the carbon and oxygen maps [Figure 6(D,F), respectively] indicate the presence of a tissue layer. Note that the iron wire may be used as a reference for the carbon background signal, due to the carbon coating. The iron distribution map [Figure 6(B)] demonstrates that the oxide phase is voluminous, as it extends nearly all the way around the sample in a diffuse ring approximately 100 μm in thickness. It appears that the pieces of the passive layer [Figure 6(C,E)] are at the migration front of an expanding layer of iron oxide, which is encapsulated in some type of binding matrix. There appears to be no passive layer left intact on the surface of the wire, which would lead to further corrosion.

Identification of hematite as the corrosion product with Raman Spectroscopy and EDS

Corroded iron wires from both experimental models were characterized using micro-Raman Spectroscopy and EDS. The micro-Raman analysis method has an advantage of simple sample preparation and the ability to acquire a confirming scan with minute quantities of corrosion product. The laser spot size is about 5 μm under an $\times 50$ objective lens. In certain samples, although spectroscopic spectra were noisy with weak characteristic peaks, presence and location of these peaks were still recognizable and reproducible. The weak signals were mainly due to too small quantities of iron oxides dispersed in an irregular biological tissue.

Several locations on each of the samples were scanned using both types of analysis to obtain more consistent results. The EDS analysis detected the presence of iron, oxygen, phosphorous, calcium, and potassium (Supporting Information Figure S1). The phosphorous and calcium may have been detected due to the presence of tissue or as a mineralized passive layer present on the surface of the sample. Phosphorous, calcium, and potassium may also have been incorporated into the corrosion product(s). The low-atomic percent of iron in the spectrum was most likely caused by interference from the tissue on the surface.

The Raman spectrum for the wire implants from within the artery wall showed peaks at $\sim$213 cm^{-1} and $\sim$277 cm^{-1} [Figure 7(A)]. Similarly, the luminal implanted wires revealed characteristic peaks at $\sim$215 cm^{-1} and $\sim$278 cm^{-1} [Figure 7(B)]. The characteristic peaks for both samples were compared with the Raman spectrum of hematite (Supporting Information Figure S2).[23] The peaks from the test samples resemble the two largest characteristic peaks of hematite located at 225 cm^{-1} and 291 cm^{-1}. It is apparent that a shift in the spectrum occurred, a possible result of interference from retained biological material on the surface of the sample or, most likely, an artifact of the laser power used to generate the spectrum (see Appendix). The shift to lower wavenumber is accounted for the anharmonic vibration of the crystal lattice by higher laser power.

As presented in Figure 7(C), magnetite signal at 663cm^{-1} could also be found in some areas of the luminal implanted specimens. Magnetite has a prominent characteristic peak at $\sim$661 cm^{-1} (Supporting Information Figure S3).[24]

Overall, Raman spectroscopy has proven to be a viable method for determining *in vivo* corrosion products. The capabilities of Raman spectroscopy supersede the limitation of most other analysis methods that require large quantities of product to obtain a confirming spectrum. However, the presence of tissue or biomaterials on the sample or a high-laser power may cause complications because residual biomaterial may absorb energy from the signal and the laser may cause sample degradation, which can shift the peak locations on the spectrum. Furthermore, subsequent studies may utilize mass spectrophotometry to help identify the corrosion products that migrate into the tissue.

DISCUSSION

We have demonstrated the feasibility of a biodegradable metallic wire implanted into a rat artery to serve as an experimental model to investigate the corrosion behavior of biodegradable stent materials. Although the geometry of a wire is not the same as a stent, this model allows for detailed investigations at the interface between the candidate metal and the arterial blood or wall matrix. This experimental model may serve as a prescreening assay for candidate stent materials before stent manufacturing and large animal studies. Although the iron wire used in the experiments was only 20 mm long and 0.25 mm in diameter, we were able to assess surface topography, identify corrosion products, and characterize corrosion product diffusion with conventional approaches. We identified the corrosion product formed around the near pure iron material as the iron oxide hematite and found that the hematite particles spread from the wire in a manner that depended on the characteristics of the contacting biological material. We showed that immediate encapsulation of iron or magnesium wires within the arterial wall was conducive to corrosion, whereas wires implanted into the arterial lumen in contact with flowing arterial blood experienced minimal corrosion. Corrosion products from the iron wire accumulated over 9 months and were retained in the arterial wall as voluminous flakes that threatened the integrity of the arterial wall. Although magnesium corroded more rapidly than the iron, there was no visible retention of corrosion products within the vessel wall. The similar regulation of iron and magnesium corrosion by the host environment suggests that corrosion resistance may be a general property of biodegradable metals placed in contact with flowing arterial blood and corrosion in the arterial wall may be caused by arterial wall constituents, such as vascular matrix, vascular cells, or due to the absence of contacting arterial blood. In contrast to magnesium and iron, conventional stents are constructed from corrosion resistant alloys.[1–3,25]

We selected iron as the initial material to demonstrate the capability of the novel experimental model because iron material has been used previously to construct experimental stents, and there have been several reports on the corrosion process of pure iron in the arterial environment,[16,21] allowing us to focus on developing the new animal model and associated methodology for biomaterial microanalysis. The present model does not simulate all aspects of stent/artery interaction, such as forces between the artery/implant and mechanical stretch-related injury to the arterial wall. A further limitation is that the wire implantation requires piercing the aorta and producing injury/inflammation, which may influence the ensuing corrosion process. The animal model also lacks atherosclerotic lesions, which may contain considerable calcium, phenotypically modulated smooth muscle cells, and dysfunctional endothelial cells. However, the benefit of the rodent wire implantation approach relative to a large animal stent implantation is that it can be used to quickly and with low-cost evaluate the corrosion behavior of novel stent materials for prescreening before materials processing, stent manufacturing development, and large animal implantation studies. This provides an opportunity to gather initial observations into material degradation behavior that can be used to assess the technical feasibility to warrant continued investment in more thorough experimentation. Thus, we have developed a novel model for rapid prescreening of candidate stent materials and demonstrated the capability of the model to assess biocorrosion in the arterial environment.

We found that arterial matrix-contacting iron or magnesium wires experienced substantial biocorrosion relative to iron or magnesium wires that contacted flowing arterial blood. The mechanism for corrosion in the arterial wall is not clear. Corrosion may be due to differences in the ionic, cellular, or material environments of the arterial wall

relative to arterial blood. The ion-rich blood may act to passivate the metallic surface and protect the wire from corrosion, whereas wires in the wall may passivate to a lesser extent or may not be protected by the passive layer. If more phosphate is present in one environment relative to another, for example, the potential for phosphate surface mineralization is greater. In fact, a calcium and phosphate-rich layer was recorded on the implanted iron wire. Alternatively, there may be greater exposure to ionic iron or magnesium (in the blood) than in the tissue, and thus less of an electrochemical potential for corrosion. Unfortunately, the corrosion mechanism can be difficult to clarify *in vivo* due to the complex cellular and material composition of the arterial wall and the ionic composition of arterial blood. The arterial wall contains a complex, electrically charged matrix material, along with vascular cells within the layers of the wall, both of which may regulate ionic concentrations on the surface of the implanted metal. Negatively charged proteoglycans present in the arterial matrix for example may repel phosphate ions and thereby impede the formation of a protective phosphate layer. The extracellular matrix may regulate the diffusion/retention of corrosion reactants and products based on the charge and pore size of the matrix. Vascular smooth muscle cells are able to regulate their local ionic environment.[26–28] It may therefore be necessary to conduct *in vitro* studies to resolve the roles of the arterial blood, fibrous matrix, proteoglycans, and vascular cells in the corrosion process.

CONCLUSIONS

We have demonstrated the feasibility of an arterial wire implantation model by comparing the short and long-term corrosion behavior of iron, by comparing the corrosion behavior of iron and magnesium, and demonstrating the importance of the arterial environment for directing the corrosion process. We have also used this model to demonstrate that the degradation products of an iron arterial implant are retained in an expanded form that may challenge the long-term integrity of the artery, whereas magnesium degradation products are not retained in the wall. On the basis of our novel findings, we speculate that blood-contacting surfaces of a deployed iron or magnesium stent may experience reduced corrosion, whereas surfaces of the stent that are pressed against the endothelium and shielded from the blood may undergo biocorrosion. In the case of iron, the biocorrosion product may be retained within the encapsulating neointima in an expanded form that may complicate normal arterial function.

Because the chemical composition of biodegradable materials may need to be modified to improve the performance of biodegradable stents and candidate materials can be more readily assessed when formed into a wire rather than a deployable stent, the present arterial wire implantation model may be useful for developing materials with degradation properties more suitable for vascular stenting applications.

REFERENCES

1. Camenzind E. Treatment of in-stent restenosis—Back to the future? N Engl J Med 2006;355:2149–2151.
2. Kastrati A, Mehilli J, Pache J, Kaiser C, Valgimigli M, Kelbaek H, Menichelli M, Sabate M, Suttorp MJ, Baumgart D, Seyfarth M, Pfisterer ME, Schomig A. Analysis of 14 trials comparing sirolimus-eluting stents with bare-metal stents. N Engl J Med 2007; 356:1030–1039.
3. Koster R, Vieluf D, Kiehn M, Sommerauer M, Kahler J, Baldus S, Meinertz T, Hamm CW. Nickel and molybdenum contact allergies in patients with coronary in-stent restenosis. Lancet 2000;356: 1895–1897.
4. Yun YH, Dong ZY, Lee N, Liu YJ, Xue DC, Guo XF, Kuhlmann J, Doepke A, Halsall HB, Heineman W, Sundaramurthy S, Schulz MJ, Yin ZZ, Shanov V, Hurd D, Nagy P, Li WF, Fox C. Revolutionizing biodegradable metals. Mater Today 2009;12:22–32.
5. Ramcharitar S, Serruys PW. Fully biodegradable coronary stents progress to date. Am J Cardiovasc Drugs 2008;8:305–314.
6. Colombo A, Karvouni E. Biodegradable stents—"Fulfilling the mission and stepping away". Circulation 2000;102:371–373.
7. Erne P, Schier M, Resink TJ. The road to bioabsorbable stents: Reaching clinical reality? Cardiovasc Intervent Radiol 2006;29: 11–16.
8. Hermawan H, Dube D, Mantovani D. Developments in metallic biodegradable stents. Acta Biomater 2010;6:1693–1697.
9. Eggebrecht H, Rodermann J, Hunold P, Schmermund A, Bose D, Haude M, Erbel R. Novel magnetic resonance-compatible coronary stent—The absorbable magnesium-alloy stent. Circulation 2005;112:E303–E304.
10. Erbel R, Di Mario C, Bartunek J, Bonnier J, de Bruyne B, Eberli FR, Erne P, Haude M, Heublein B, Horrigan M, Ilsley C, Bose D, Koolen J, Luscher TF, Weissman N, Waksman R. Temporary scaffolding of coronary arteries with bioabsorbable magnesium stents: A prospective, non-randomised multicentre trial. Lancet 2007;369:1869–1875.
11. Waksman R, Pakala R, Kuchulakanti PK, Baffour R, Hellinga D, Seabron R, Tio FO, Wittchow E, Hartwig S, Harder C, Rohde R, Heublein B, Andreae A, Waldmann KH, Haverich A. Safety and efficacy of bioabsorbable magnesium alloy stents in porcine coronary arteries. Catheter Cardiovasc Interv 2006;68:607–617.
12. Heublein B, Rohde R, Kaese V, Niemeyer M, Hartung W, Haverich A. Biocorrosion of magnesium alloys: A new principle in cardiovascular implant technology? Heart 2003;89:651–656.
13. Grube E, Sonoda S, Ikeno F, Honda Y, Kar S, Chan C, Gerckens U, Lansky AJ, Fitzgerald PJ. Six- and twelve-month results from first human experience using everolimus-eluting stents with bioabsorbable polymer. Circulation 2004;109:2168–2171.
14. Tamai H, Igaki K, Kyo E, Kosuga K, Kawashima A, Matsui S, Komori H, Tsuji T, Motohara S, Uehata H. Initial and 6-month results of biodegradable poly-L-lactic acid coronary stents in humans. Circulation 2000;102:399–404.
15. Middleton JC, Tipton AJ. Synthetic biodegradable polymers as orthopedic devices. Biomaterials 2000;21:2335–2346.
16. Peuster M, Hesse C, Schloo T, Fink C, Beerbaum P, von Schnakenburg C. Long-term biocompatibility of a corrodible peripheral iron stent in the porcine descending aorta. Biomaterials 2006;27: 4955–4962.
17. Moravej M, Prima F, Fiset M, Mantovani D. Electroformed iron as new biomaterial for degradable stents: Development process and structure–properties relationship. Acta Biomater 2010;6:1726– 1735.
18. Moravej M, Purnama A, Fiset M, Couet J, Mantovani D. Electroformed pure iron as a new biomaterial for degradable stents: In vitro degradation and preliminary cell viability studies. Acta Biomater 2010;6:1843–1851.
19. Hermawan H, Dube D, Mantovani D. Degradable metallic biomaterials: Design and development of Fe–Mn alloys for stents. J Biomed Mater Res A 2010;93A:1–11.
20. di Mario C, Griffiths H, Goktekin O, Peeters N, Verbist J, Bosiers M, Deloose K, Heublein B, Rohde R, Kasese V, Isley C, Erbel R. Drug-eluting bioabsorbable magnesium stent. J Interv Cardiol 2004;17:391–395.
21. Waksman R, Pakala R, Baffour R, Seabron R, Hellinga D, Tio FO. Short-term effects of biocorrodible iron stents in porcine coronary arteries. J Interv Cardiol 2008;21:15–20.

22. Peuster M, Wohlsein P, Brugmann M, Ehlerding M, Seidler K, Fink C, Brauer H, Fischer A, Hausdorf G. A novel approach to temporary stenting: Degradable cardiovascular stents produced from corrodible metal—Results 6–18 months after implantation into New Zealand white rabbits. Heart 2001;86:563–569.
23. Schlepp E. 2010. Hematite R050300-RRUFF Database: Raman, X-ray, Infrared, and Chemistry. http://rruff.info/hematite/display=default/R050300.
24. Scott M.2010. Magnetite R061111—RRUFF Database: Raman, X-ray, Infrared, and Chemistry. http://rruff.info/hematite/display=default/R061111.
25. Singh R, Dahotre NB. Corrosion degradation and prevention by surface modification of biometallic materials. J Mater Sci Mater Med 2007;18:725–751.
26. Giachelli CM. The emerging role of phosphate in vascular calcification. Kidney Int 2009;75:890–897.
27. Li X, Yang HY, Giachelli CM. Role of the sodium-dependent phosphate cotransporter. Pit-1, in vascular smooth muscle cell calcification. Circ Res 2006;98:905–912.
28. Jono S, McKee MD, Murry CE, Shioi A, Nishizawa Y, Mori K, Morii H, Giachelli CM. Phosphate regulation of vascular smooth muscle cell calcification. Circ Res 2000;87:E10–E17.
29. deFaria DLA, Silva SV, deOliveira MT. Raman microspectroscopy of some iron oxides and oxyhydroxides. J Raman Spectrosc 1997;28:873–878.
30. Oh SJ, Cook DC, Townsend HE. Characterization of iron oxides commonly formed as corrosion products on steel. Hyperfine Inter 1998;112:59–65.
31. Bersani D, Lottici PP, Montenero A. Micro-Raman investigation of iron oxide films and powders produced by sol–gel syntheses. J Raman Spectrosc 1999;30:355–360.
32. Hanesch M. Raman spectroscopy of iron oxides and (oxy)hydroxides at low laser power and possible applications in environmental magnetic studies. Geophys J Int 2009;177:941–948.
33. Larroumet D, Greenfield D, Akid R, Yarwood J. Raman spectroscopic studies of the corrosion of model iron electrodes in sodium chloride solution. J Raman Spectrosc 2007;38:1577–1585.

APPENDIX

Raman Spectroscopy of Iron Oxides

Raman spectroscopy is useful to distinguish different iron oxides and oxyhydroxides compounds in rust composition.[29,30] Various iron oxides and hydroxides have received a lot of interest as corrosion products of steels, and the Raman spectra are used as fingerprints to detect particular species.[31] The most common iron oxides and hydroxides are hematite (α-Fe_2O_3), maghemite (β-Fe_2O_3), magnetite (Fe_3O_4), and goethite (α-FeOOH). Although it was claimed that iron oxides and hydroxides were poor light scatters,[29,32] it was possible to characterize and distinguish these powders reliably at low-laser powers. In fact, low-laser power should be used to avoid sample degradation, which usually occurs under intense laser illumination and may lead to misinterpretation of the spectra. Due to the small size of our wire sample, micro-Raman spectroscopy was used in this study to characterize the corroded implant materials.

As reported in the literature,[29,32,33] iron oxides were usually studied using low-laser power (1–2 mW) to avoid sample degradation. We therefore use a commercial available Fe_2O_3 powder (purchased from Alfa Aesar CAS# 1309-37-1) as our reference to identify the effect of laser power to the sample. As shown in Figure 8(a), raising the laser power from 0.17 mW to 8.5 mW broadens the Raman bands and shifts them to lower wavenumbers. Figure 8(b) presents the correlation between laser power and position of two characteristic peaks to reveal the trend.

From our investigation, we note that low-laser power is necessary to characterize iron oxides properly. We confirmed that high-laser power could cause localized heating to the sample and therefore induce anharmonic vibration to the crystal lattice. In our Raman system, a full power of 17 mW can even damage the sample and give rise to a strong background signal with no characteristic Raman peaks. Reduced laser power, typically 4–8 mW, was used to minimize the risks of spectral misinterpretation due to sample degradation. We also suggest that cooling the sample to lower temperature may be helpful.

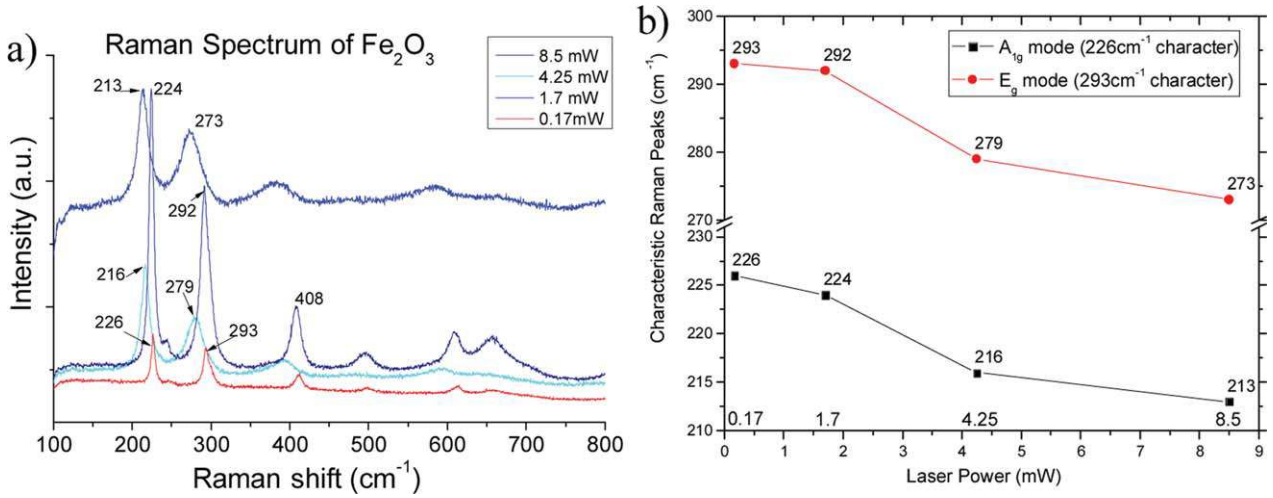

FIGURE 8. (a) Raman spectrum of hematite with different laser power. (b) Correlation between the laser power and the peaks position. [Color figure can be viewed in the online issue, which is available at wileyonlinelibrary.com.]